Supplementary Information for

Robust Structural Superlubricity under Gigapascal Pressures

This supplementary information contains Supplementary Notes on

1. Determination of the contact pressure

2. Friction of SSL in graphite under high pressure

3. Breakdown pressure at the graphite/tungsten contact

4. Breakdown pressure at the defective graphite/graphite contact

5. Shear-lag model analysis of tearing of the graphite layers

6. Simulation movies of the step-wear mechanisms

and Supplementary Figures S1-S9 and Tables S1-S2.

1. Determination of the contact pressure

1.1 The graphite/graphite contact

The contact pressure of the graphite/graphite contact was calculated using the finite element analysis (FEA) (**Fig. S1a**). Graphite is modeled as a linear transversely-isotropic solid. The stress-strain relation is [1,2]

$$\begin{bmatrix} \sigma_x \\ \sigma_y \\ \sigma_z \\ \tau_{xy} \\ \tau_{xz} \\ \tau_{yz} \end{bmatrix} = \begin{bmatrix} 1060 & 180 & 15 & 0 & 0 & 0 \\ 180 & 1060 & 15 & 0 & 0 & 0 \\ 15 & 15 & 36.5 & 0 & 0 & 0 \\ 0 & 0 & 0 & 440 & 0 & 0 \\ 0 & 0 & 0 & 0 & 4.5 & 0 \\ 0 & 0 & 0 & 0 & 0 & 4.5 \end{bmatrix} \begin{bmatrix} \varepsilon_x \\ \varepsilon_y \\ \varepsilon_z \\ \gamma_{xy} \\ \gamma_{xz} \\ \gamma_{yz} \end{bmatrix}$$

where σ (τ) and ε (γ) are the stress and the strain of the material, respectively.

A linear elastic cohesive model is applied to describe the interaction at the graphite/graphite contact (**Fig. S1b**). The stiffness of the adhesion (stress versus interlayer distance) is K_{nn} = 11.11 GPa/nm, which is derived from the Lennard-Jones potential that is widely used to describe the vdW interaction [2]. Breakdown of the traction is activated when the adhesion stress exceeds 0.4 GPa. The shear strength of the graphite/graphite interface is τ_s = 57 kPa [3]. Other contacts are tied in FEA for simplicity. A 3D solid element (C3D8) was applied for meshing. The mesh is refined at the contact area to ensure the convergence of numerical calculations. The width of each element is 0.5 percent of the tip radius. At least 4 elements are meshed across the thickness. Thickness of the graphite mesa and the mechanically exfoliated graphite substrate were characterized by using the atomic force microscope (AFM, see **Fig. S2**). The graphite mesa contains a 100 nm-thick SiO_2 cap of and a 50 nm-thick graphite layer, and the graphite substrate is 20 nm-thick. Radius of the tungsten tip (3.5 μm) was characterized by using the scanning electron microscope (SEM). The maximum contact pressure calculated at the graphite/graphite contact under the highest accessible load of 10 mN is 9.45 GPa. The pressure distribution indicates an effective contact radius of ~0.8 μm (**Fig. S3**).

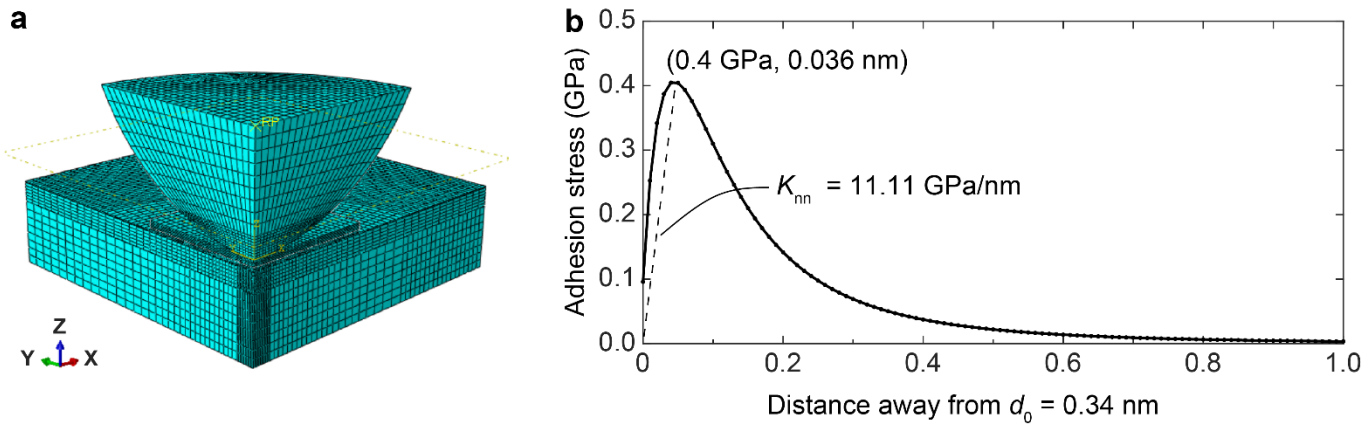

Fig. S1. FEA model of the graphite/graphite contact. (a) Meshes of the FEA model using the 3D solid element C3D8. (b) The linear elastic cohesive model for the interaction at the graphite/graphite contact [2]. K_{nn} is the stiffness of the adhesion (stress versus the interlayer distance away from the equilibrium position between adjacent graphene layers denoted as d_0 = 0.34 nm). Breakdown of the traction is activated as the adhesion stress exceeds 0.4 GPa (0.036 nm away from d_0).

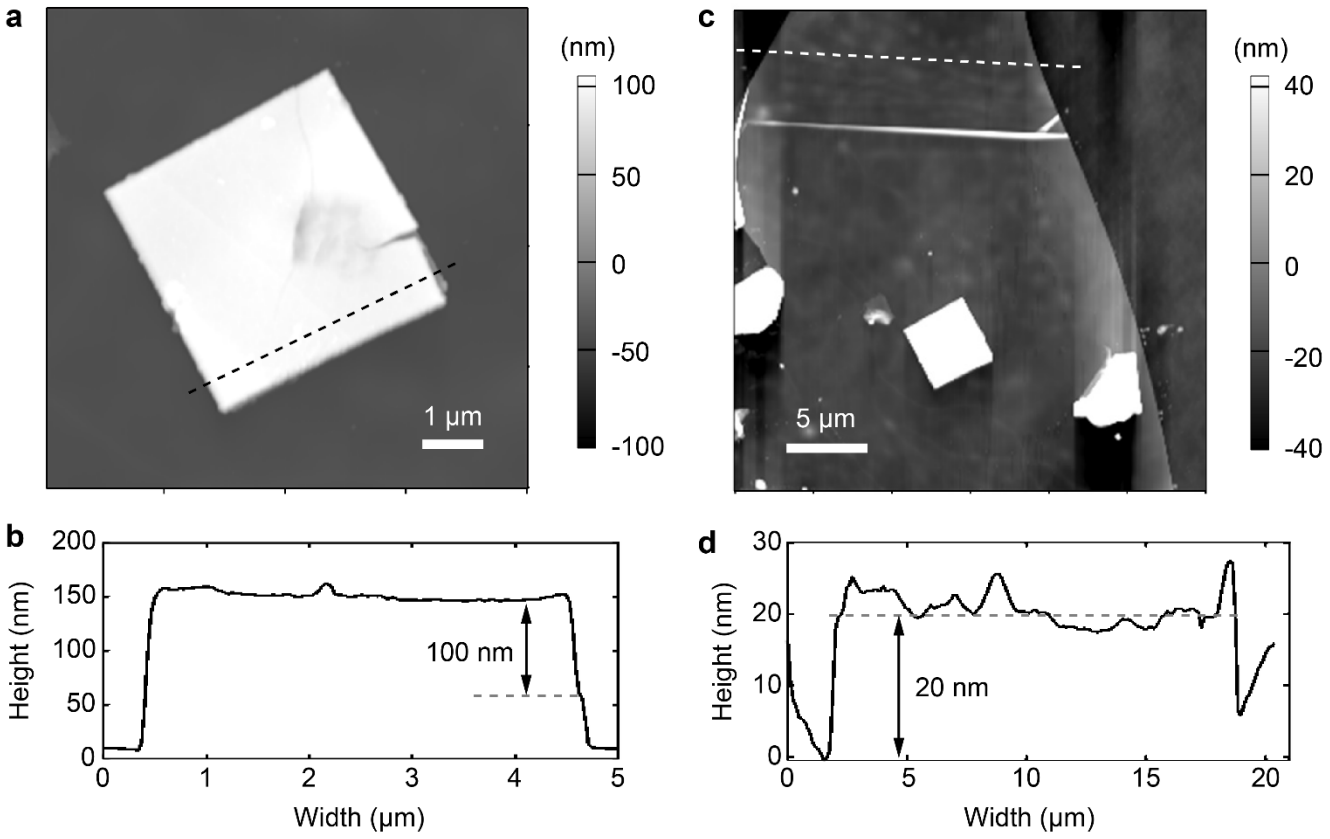

Fig. S2. AFM characterization of the thickness of graphite samples. (a, b) Characterization of the graphite mesa. The mesa contains a 100 nm-thick SiO_2 cap and a 50 nm-thick graphite layer. (c, d) Characterization of the graphite substrate. The thickness of the graphite substrate is 20 nm.

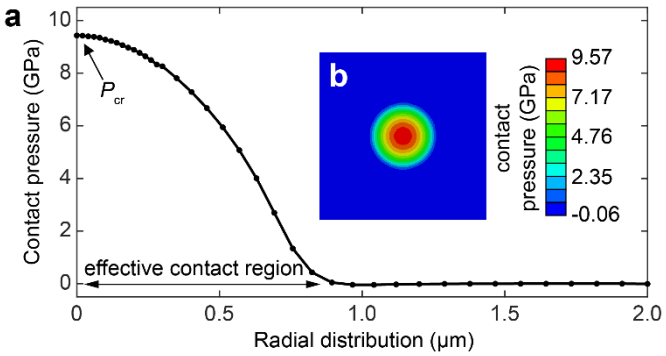

Fig. S3. Contact pressure at the graphite/graphite contact under the normal load of 10 mN. (a) Radial distribution of the contact pressure. (b) Contour map of the contact pressure.

1.2 The graphite/tungsten contact

The contact pressure of the graphite/tungsten contact is calculated by using the Hertz model [4]

$$\frac{1}{E}=\frac{1-v_1^2}{E_1}+\frac{1-v_2^2}{E_2}, \tag{1}$$

$$a=(\frac{3WR}{4E})^{\frac{1}{3}}, \tag{2}$$

$$P=\frac{3W}{2\pi a^2}, \tag{3}$$

where E_1 = 405 GPa (v_1 = 0.28) and E_2 = 73 GPa (v_2 = 0.17) [2] are the elastic modulus (Poisson's ratio) of the tungsten tip and substrate, respectively. W is the normal load applied to the graphite substrate, R is the radius of the tip, a is the radius of the effective contact region as defined in **Eq. 2** (see **Fig. S4a**), and P is the maximum contact pressure in the contact region. Herein, the substrate is regarded as silica (the oxide layer on top of the bulk silicon, see **Fig. S4a**), since the thickness of the graphite layer (~10 nm) is much smaller than that of the silica film (~300 nm). The assumption is validated by the FEA, where the contact models with and without the graphite layer are both calculated. The result shows a difference of 3% for the contact pressure. Radius of the tip (~ 1.75 μm) was characterized by the OM (**Fig. S4b**). Parameters characterized for the samples are listed in **Table S1**.

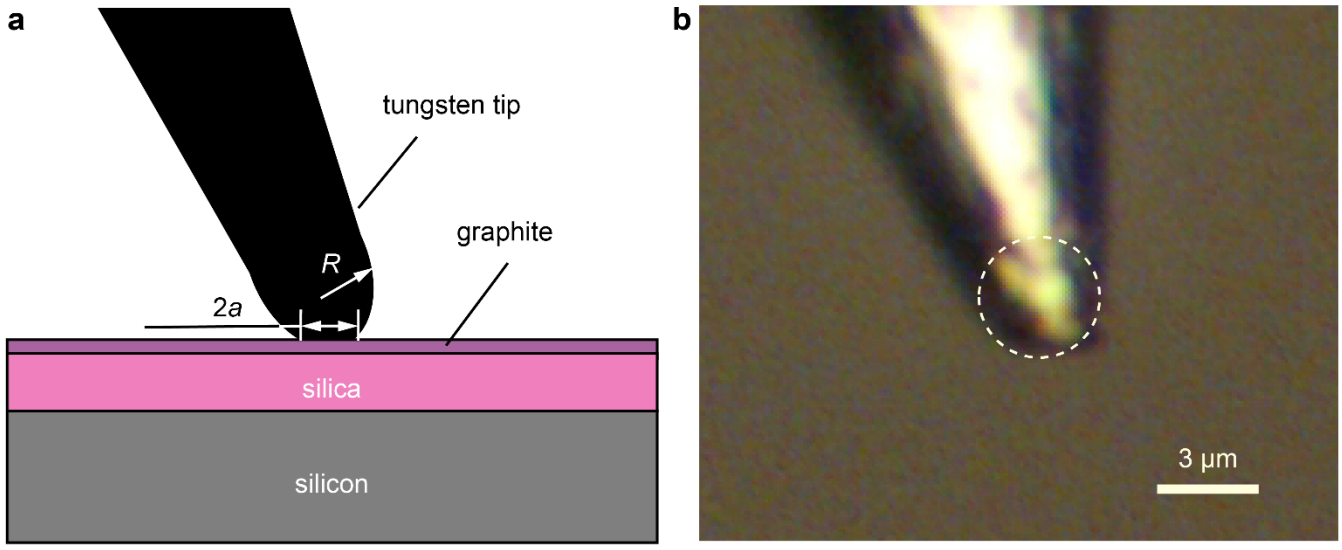

Fig. S4. Characterization of the graphite/tungsten contact. (a) Schematic of the contact. (b) An OM image of the tungsten tip with the radius of ~1.75 μm.

Table S1. Parameters and the maximum pressure of the graphite/tungsten contact.

R (μm)	W (mN)	P (GPa)	a (μm)
1.75	0.3	3.74	0.16
	0.5	5.07	0.22

2. Friction of SSL in graphite under high pressures

Friction of SSL at the graphite/graphite interface under high pressure was measured by using a home-build two-dimensional force sensor [5]. The friction force was calculated as the area enclosed in the friction loop divided by the sliding distance (**Fig. S5a-d**). Friction behaviors of the graphite/graphite contact were investigated under normal loads ranging from 0.25 mN to 2.5 mN, which correspond to pressure from 1.46 GPa to 5.72 GPa. The load is limited by the range of the force sensor. The friction coefficient is ~10^{-4} (the change of the friction force versus the change of the normal load, see **Fig. 1f**), which represents a stable SSL state within pressure of a few gigapascals. Notably, previous studies found that the edge of the mesa/substrate contact contributes the most to the friction force [6], whereas the friction force of the interior region of the contact is nearly zero and remains unchanged under variable pressure, indicating SSL.

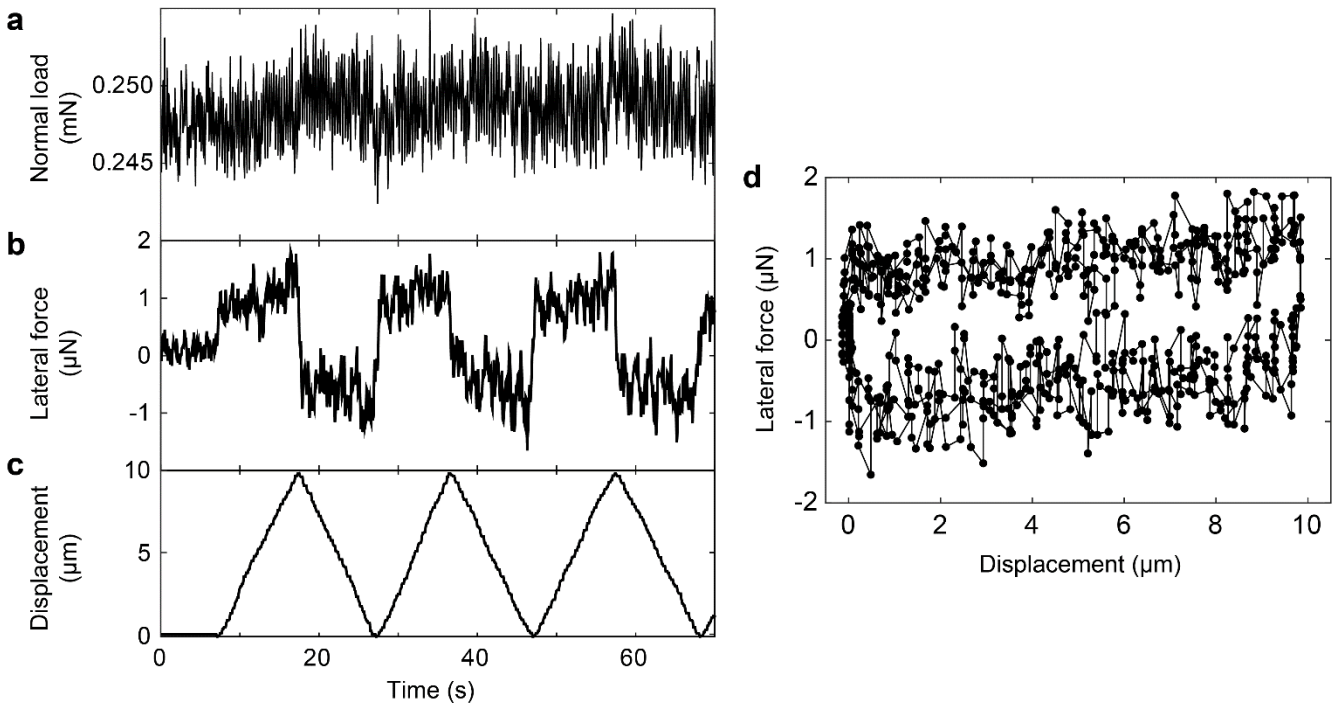

Fig. S5. Friction measurement of at the graphite SSL constact. (a-c) Normal loads and lateral forces measured by using a home-build two-dimensional force sensor during movement of the graphite substrate. (d) Friction loops enclosed by the lateral forces and sliding distance in forward and backward sliding directions.

3. Breakdown pressure at the graphite/tungsten contact

Six samples of graphite/tungsten contacts were prepared for the determination of the breakdown pressure (P_{cr}). For each sample, normal loads were increased subsequently. Under each load, the tip slid for only one cycle before wear was checked. The sliding distance and velocity in all experiments are 30 μm and 10 μm/s, respectively. The value of P_{cr} varies from 3.44 to 12.12 GPa with an average value of 7.34 GPa, which is defined as the maximum contact pressure when a wear event is firstly detected (**Table S2**).

Table S2. Parameters and the critical pressure of the graphite/tungsten contact.

#No.	R (μm)	W (mN)	P_{cr} (GPa)	a (μm)
1	4.43	1	3.44	0.37
2	1.5	0.3	4.74	0.17
3	1.19	0.5	6.56	0.19
4	2.27	2	6.77	0.38
5	1.19	2	10.41	0.3
6	1.16	3	12.12	0.34

4. Breakdown pressure at the defective graphite/graphite contact

The breakdown pressure for the defect-free graphite/graphite contact is higher than the maximum accessible pressure in our experiments. To study wear characteristics of the graphite/graphite contact, material imperfections were introduced into the graphite substrate by using the argon plasma under a power of 2 W and a time duration of 10 s before transferring a graphite mesa on it. The argon plasma treatment could add defects into the SSL system without introducing other chemical species [7]. Raman spectrum characterization was conducted to check the implantation of defects, which shows a detectable intensity of the defective graphene peak at 1350 cm^{-1}(**Fig. S6**).

Experimental setup of defective graphite/graphite contacts, following that of the defect-free graphite/graphite contact. The sliding distance and velocity is 10 μm and 10 μm/s, respectively. The surface morphology of the defective graphite substrate after sliding tests was characterized by AFM and shown in **Fig. S7**. Rupture of the graphite substrate occurred inside the track under a normal pressure of 0.4 GPa. Compared to the ultrahigh breakdown pressure (>9.45 GPa) for the defect-free graphite/graphite contact, wear nucleates easily at the defective graphite/graphite contact. As shown in **Fig. S7a**, wear nucleates at multiple locations inside the sliding track, finally evolving into tearing patterns at each site of nucleation (**Fig. S7c**).

To explain the experimental results, a contact model between tungsten and graphite with single vacancy defect was conducted for the first-principles calculations (**Fig. S8a**). As shown in **Fig. S8b**, the breakdown pressure is reduced to 0.23 GPa. The result indicates that defects play an important role in the breakdown pressure of SSL.

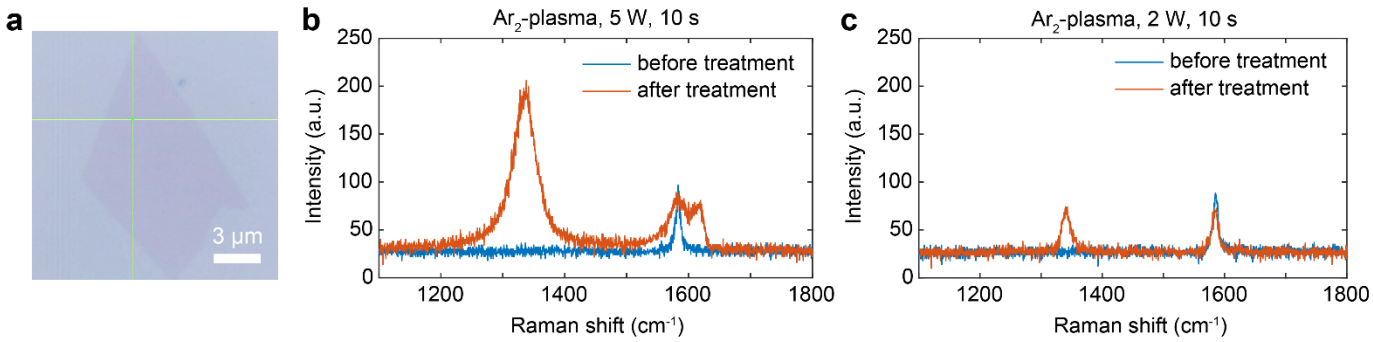

Fig. S6. Defects in graphene sheets induced by the argon plasma. (a) An OM image of the graphene sheet. (b, c) Raman spectra of samples obtained under argon-plasma treatment of 5 W, 10 s and 2 W, 10 s, respectively.

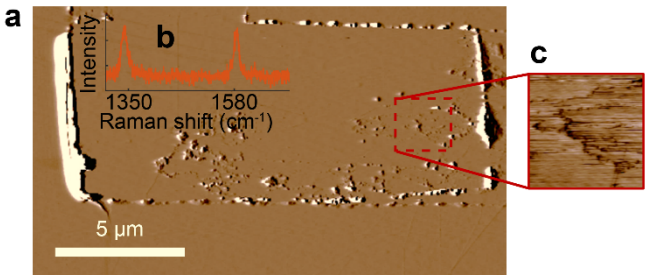

Fig. S7. Wear testing of the defective graphite/graphite contact. (a) AFM characterization of the morphology of a defective graphite substrate after a sliding test under a pressure of 0.4 GPa. Rupture of the graphite substrate occurred inside the track. (b) Raman characterization of the plasma-treated graphite substrate before transferring the graphite mesa on it. (c) The magnified view of the red box in (a), showing the tearing patterns at each site of wear nucleation.

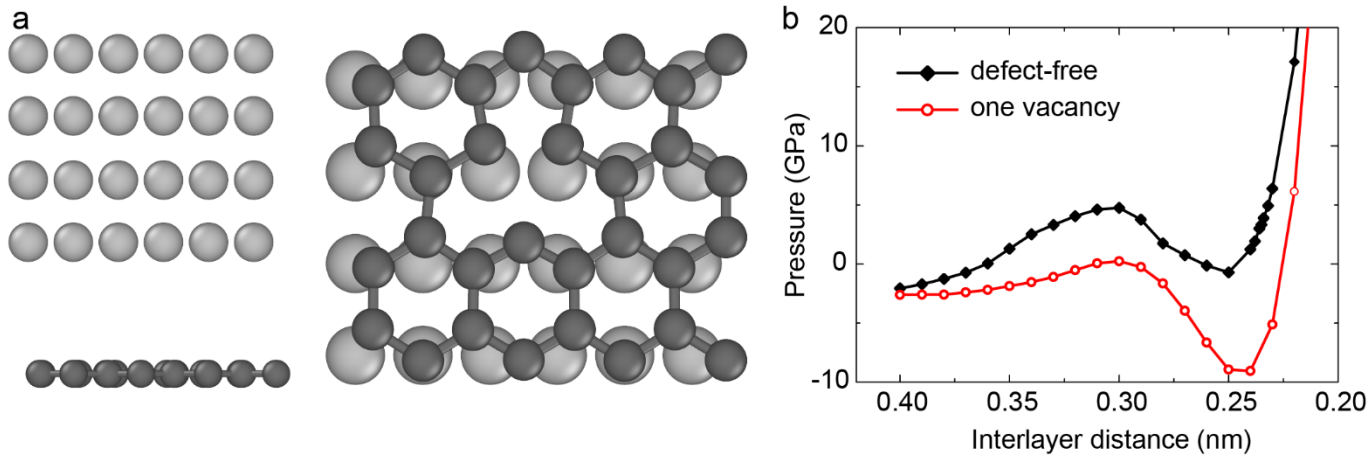

Fig. S8. DFT calculations of the graphite/tungsten contact with and without a vacancy. Side and bottom views of (a) the graphite/tungsten contact with a vacancy at the surface layer of graphite. (b) Pressure-interlayer distance relations of the defective and defect-free graphite/tungsten contacts.

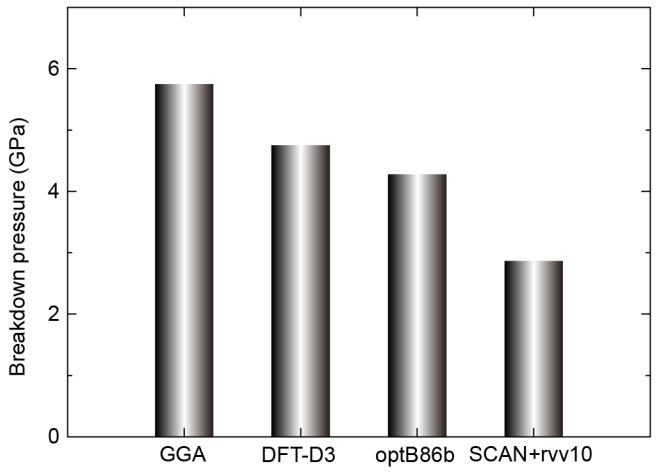

Fig. S9. DFT calculations of the breakdown pressure of the graphite/tungsten contact, using exchange-correlation functionals of GGA [8], DFT-D3 [9], optB86b-vdW [10], SCAN+rvv10 [11], respectively.

5. Shear-lag model analysis of tearing of the graphite layers

As the interlayer frictional strength of graphite (τ_b = 40 kPa)[12] is much lower than that of the bonded graphite/tungsten contact (τ_a = 5.21 GPa), the shear load transferred between the topmost layer and the rest of graphite can be neglected. Hence, a critical contact size can be determined as

$$l_c = \sigma t/\tau_a = 7.83 \text{ nm}, \quad (4)$$

where σ = 120 GPa and t = 0.34 nm are the tensile strength and the interlayer spacing of graphite, respectively. As the contact size is significantly below or above l_c, it can be predicted that there are two different modes of failure or deformation. MD simulations show that as the size of contact (8.26 nm) exceeds l_c, graphene will be teared due to the shear-induced in-plane tensile deformation (see **Movie S3** for details). However, as the size of contact (4.06 nm) is below l_c, the interfacial carbon-tungsten bonds break due to the insufficient area of load transfer at the contact. Since the contact size in experiments was estimated as a few hundred nanometers, which is much larger than l_c, the tearing of graphite layers during the sliding of graphite/tungsten contact is expected.

6. Simulation movies of the step-wear mechanisms

Movie S1. The pressure-displacement curve and simulation snapshots of the pressing process for graphite/tungsten contact.

Movie S2. The friction stress-displacement curve and simulation snapshots of the friction process.

Movie S3. Molecular dynamics simulation snapshots of the wear process.

References

1. Wang, L. F. & Zheng, Q. S. Extreme anisotropy of graphite and single-walled carbon nanotube bundles. *Appl. Phys. Lett.* **90**, 153113 (2007).
2. Liu, Z. *et al.* Interlayer binding energy of graphite: A mesoscopic determination from deformation. *Phys. Rev. B* **85**, 205418 (2012).
3. Vu, C. C. *et al.* Observation of normal-force-independent superlubricity in mesoscopic graphite contacts. *Phys. Rev. B* **94**, 081405 (2016).
4. Wen, S. Z. & Huang, P. *Principles of Tribology*. 192-195 (Tsinghua University Press, 1990).
5. Sun, T. T., Wu, Z. H., Li, Z. H., Zheng, Q. S. & Lin, L. A hybrid two-axis force sensor for the mesoscopic structural superlubricity studies. *Sensors* **19**, 3431 (2019).
6. Qu, C. Y. *et al.* Origin of friction in superlubric graphite contacts. *Phys. Rev. Lett.* **125**, 126102 (2020).
7. Eckmann, A. *et al.* Probing the nature of defects in graphene by raman spectroscopy. *Nano Lett.* **12**, 3925-3930 (2012).
8. Perdew, J. P., Burke, K. & Ernzerhof, M. Generalized gradient approximation made simple. *Phys. Rev. Lett.* **77**, 3865-3868 (1996).
9. Grimme, S., Antony, J., Ehrlich, S. & Krieg, H. A consistent and accurate *ab initio* parametrization of density functional dispersion correction (DFT-D) for the 94 elements H-Pu. *The Journal of Chemical Physics* **132**, 154104 (2010).
10. Klimeš, J., Bowler, D. R. & Michaelides, A. Chemical accuracy for the van der Waals density functional. *J. Phys.: Condens. Matter* **22**, 022201 (2009).
11. Peng, H., Yang, Z.-H., Perdew, J. P. & Sun, J. Versatile van der Waals density functional based on a meta-generalized gradient approximation. *Phys. Rev. X* **6**, 041005 (2016).
12. Wang, G. R. *et al.* Measuring interlayer shear stress in bilayer graphene. *Phys. Rev. Lett.* **119**, 036101 (2017).